Experimental realization of type-II Weyl state in noncentrosymmetric TaIrTe$_4$

E. Haubold,[1] K. Koepernik,[1] D. Efremov,[1] S. Khim,[1,2] A. Fedorov,[1,3] Y. Kushnirenko,[1] J. van den Brink,[1,4] S. Wurmehl,[1,4]
B. Büchner,[1,4] T. K. Kim,[5] M. Hoesch,[5] K. Sumida,[6] K. Taguchi,[6] T. Yoshikawa,[6] A. Kimura,[6] T. Okuda,[7] and S. V. Borisenko[1]

[1]*IFW Dresden, Helmholtzstraße 20, 01069 Dresden, Germany*

[2]*Max-Planck-Institut für Chemische Physik fester Stoffe, Nöthnitzer Straße 40, 01187 Dresden, Germany*

[3]*II. Physikalisches Institut, Universität zu Köln, Zülpicher Straße 77, 50937 Köln, Germany*

[4]*Department of Physics, TU Dresden, 01062 Dresden, Germany*

[5]*Diamond Light Source, Harwell Campus, Didcot OX11 0DE, United Kingdom*

[6]*Graduate School of Science, Hiroshima University, 1-3-1 Kagamiyama, Higashi-Hiroshima 739-8526, Japan*

[7]*Hiroshima Synchrotron Radiation Center (HSRC), Hiroshima University, 2-313 Kagamiyama, Higashi-Hiroshima 739-0046, Japan*

We present experimental evidence for a type-II noncentrosymmetric Weyl state in TaIrTe$_4$ where it has been recently predicted theoretically. We find direct correspondence between angle-resolved photoemission spectroscopy data and calculated electronic structure both in the bulk and the surface, and clearly observe the exotic surface states which support the quasi-one-dimensional Fermi arcs connecting only four Weyl points. Remarkably, these electronic states are spin polarized in the direction along the arcs, thus highlighting TaIrTe$_4$ as an interesting type-II Weyl semimetal with a promising application potential.

A recent breakthrough in the search for the analogs of fundamental particles in condensed matter systems has led to experimental realizations of three-dimensional (3D) Dirac and Weyl semimetals [1–6]. The standard Weyl state occurs when nondegenerate bands cross in a single point of k space, the Weyl point. This can be realized in the materials where either time-reversal or inversion symmetry is broken [7–9]. The simplest Fermi surface of such a Weyl semimetal would consist of only two such points [7].

Recently, a new type of Weyl semimetal has been introduced and experimentally detected [6,10]. Unlike in standard type-I materials, the Weyl cone is strongly tilted, such that the Fermi surface consists now of both electronlike and holelike pockets touching in a single point, the Weyl point, which remains at the Fermi level. This qualitative distinction leads to marked differences in the thermodynamics and response to magnetic fields. For example, a chiral anomaly [11] will be observed only if the direction of the magnetic field is within the cone made by touching Fermi surfaces [10]. Moreover, the topological surface states connecting the Weyl points, Fermi arcs, should have a spin texture which could lead to exotic surface transport and contribute to extremely large magnetoresistance [12]. Thus, apart from the fundamental significance of a type-II Weyl state, the experimental realization of a material allowing one to control the direction of the conducted current with a magnetic field would be an important gain for future applications.

Several noncentrosymmetric materials have been proposed to be type-II Weyl semimetals, but in all of them the Fermi arcs between projections of multiple Weyl points either have not been observed directly or they were very close to trivial surface states, which significantly hinders the practical application of these materials [13–22].

It has been predicted [23] that TaIrTe$_4$ is a ternary Weyl semimetal of type II. The crystal structure of this material is shown in Fig. 1(a). It is a noncentrosymmetric stacked crystal with covalent bonds along the a and b axes and van der Waals bonds along the c axis, making it very suitable for experimental

techniques which require atomically clean surfaces. Extensive band-structure calculations have been performed for the bulk and two surfaces [(001) and (00$\bar{1}$) cleavage planes] of this material [23]. The Fermi surface shown in Figs. 1(b)–1(d) consists of several sheets: three dimensional and well isolated from other holelike pockets (light orange colors) and quasi-two-dimensional (2D) electronlike pockets (dark orange to red colors). It is at the boundaries of the large 3D holelike pockets where the calculations have identified two pairs of Weyl points, each connected by long Fermi arcs [23]. In the following, we will confirm the theoretical predictions and demonstrate the presence of these arcs experimentally.

TaIrTe$_4$ single crystals were grown from excess Te flux. Ta, Ir, and Te were mixed and placed in a crucible which was sealed inside a quartz tube under vacuum. The tube was heated up to 1000 °C, slowly cooled down to 700 °C, and then centrifuged to separate excess Te from the grown crystals [24]. In order to have a complete comparison between the theory and experiment in three dimensions, we have studied the single crystals of TaIrTe$_4$ by angle-resolved photoemission spectroscopy (ARPES) using synchrotron light with variable photon energies. Normal ARPES measurements were performed at beamline I05 of the Diamond Light Source using a Scienta R4000 hemispherical electron energy analyzer with an angular resolution of 0.20° and 3 meV in energy resolution. The samples were cleaved *in situ* in a vacuum lower than 2×10^{-10} mbar and were measured at temperatures between 5 and 10 K. Spin-resolved data were recorded at the ESPRESSO Spin ARPES detector at the Hiroshima Synchrotron Radiation Center. The system uses a Scienta R4000 electron energy analyzer and has two very-low-energy electron diffraction (VLEED) detectors connected to it, each able to measure spin polarization in two axes. Overall, the system is able to measure a complete 3D spin-resolved image of the material [25,26]. The band-structure calculations were obtained using the full potential local orbital code (FPLO) [27] using the setup from Ref. [23]. From the density functional theory (DFT) calculation a minimum basis Wannier function
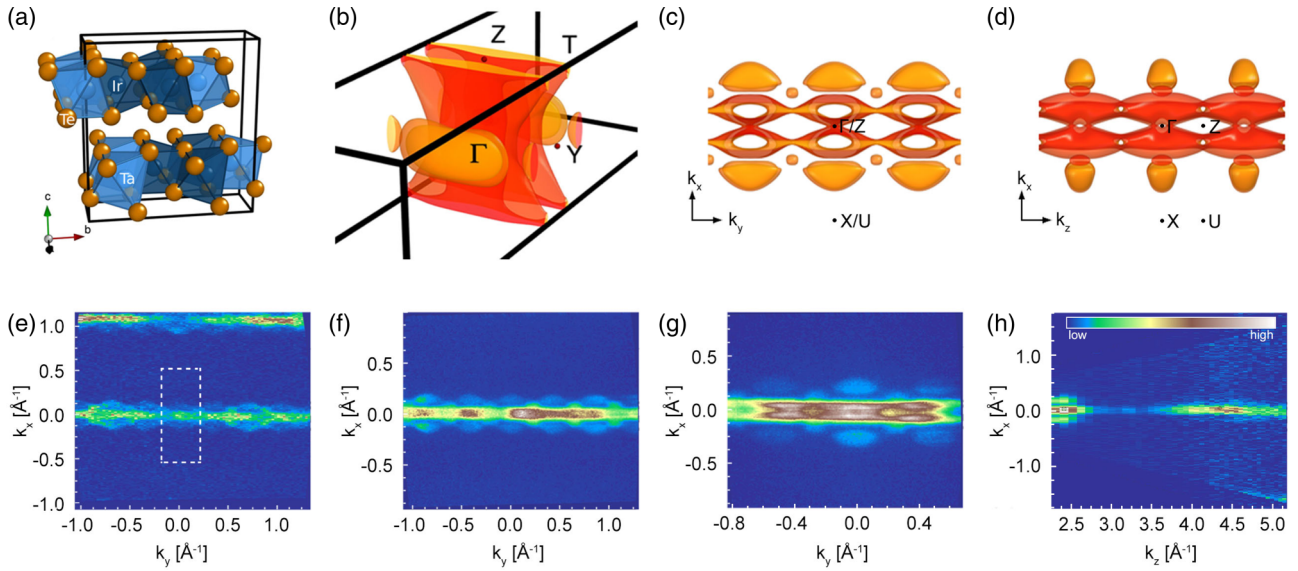
FIG. 1. (a) Crystal structure of TaIrTe$_4$. (b) Calculated 3D Fermi surface. (c) Projection to k_x-k_y plane. (d) Projection to k_x-k_z plane. ARPES Fermi surface maps taken using different photon energies: (e) 100 eV with the Brillouin zone shown as a dashed box, (f) 70 eV, and (g) 25 eV. (h) Photon energy dependent ARPES scan from 20 to 100 eV. The k_z values have been calculated using a standard procedure with an inner potential of 15 eV. A color scale used in (e)–(h) is shown as an inset.

model was extracted, which was then mapped onto a semi-infinite slab geometry whose surface spectral function was obtained via Green's function techniques.

In Figs. 1(e)–1(h) we show the ARPES Fermi surface maps measured from the cleaved (001) surface. The overview map recorded using 100 eV photons is shown in Fig. 1(e), together with the Brillouin zone (BZ). As is seen from the map, the electronic structure naturally follows the significant anisotropy of the crystal structure and is in remarkable agreement with the results of the calculations. The Fermi surface is relatively small, implying rather low concentrations of the charge carriers. Large, nonsymmetrized maps with subsequent zooming in [Figs. 1(e)–1(g)] by means of lowering the photon energy allowed us to effectively scan the electronic structure at different k_z values. While there are no large qualitative changes, the size, shape, and intensity of particular features are not constant. For example, the isolated areas almost homogeneously filled by intensity and clearly corresponding to holelike pockets [light-orange surfaces in Figs. 1(b)–1(d)] appear differently in different maps and in neighboring BZs within the same map, and in some cases are hardly observed at all.

This is in agreement with their three-dimensional character predicted by the calculations—the ARPES momentum resolution along k_z does not allow one to observe sharp contours as in the case of quasi-2D features, but its finite value still makes it possible to track the mentioned changes. We have also recorded a detailed excitation energy dependence map of the center of the Brillouin zone around the Γ point. The resulting k_x-k_z projection of the Fermi surface is shown in Fig. 1(h). There is a periodically changing intensity pattern which roughly corresponds to the calculated projection from Fig. 1(d). Quasi-two-dimensional electronlike pockets are clearly seen in all maps as well, more or less precisely mimicking the repeating arrangement from the upper panels

of Fig. 1. Thus, the experimental Fermi surface qualitatively agrees with the calculated one.

The next step is to estimate the degree of quantitative agreement between the calculations and the measured data. We present momentum-energy intensity maps, which show the underlying dispersions, in Fig. 2. A comparison of the data sets corresponding to X-Γ-X cut on the large energy scale is shown in Figs. 2(a) and 2(b). Good agreement is emphasized and correctly captured by the calculation bandwidth (∼7 eV) and the overall pattern of the numerous dispersions. A comparison on a smaller scale of hundreds of meV involves two ARPES-specific effects which need to be taken into account. First is the above-mentioned three dimensionality of TaIrTe$_4$ and the moderate k_z resolution of the method. The degree of k_z dispersion is seen from the band structure along the X-Γ-X and U-Z-U cuts [Figs. 2(c) and 2(d)]. Second is the presence of a surface which may result in the occurrence of surface states. Our calculations of the spectral function of an ideal semi-infinite slab consider both factors. In Figs. 2(e)–2(g) we show the photoemission data along the cut through the center of the BZ, together with the spectral function corresponding to the two opposite surfaces. Although the overall agreement is striking, a closer inspection reveals the differences in the vicinity of the Fermi level: The crossing of the linear dispersions in the experiment occurs at lower binding energies and the corresponding fine structure is not present/resolved. This observation implies that still higher-resolution data are needed to figure out, e.g., which surface is probed and whether the surface states are present.

To further quantify the discrepancies between the theory and experiment for easier identification of the Weyl points and arcs, we analyzed the data taken with the lower photon energies which guarantee better energy and momentum resolutions. We compare more rigorously the calculated and experimental Fermi surfaces (FSs) in Fig. 3. A high-resolution Fermi surface
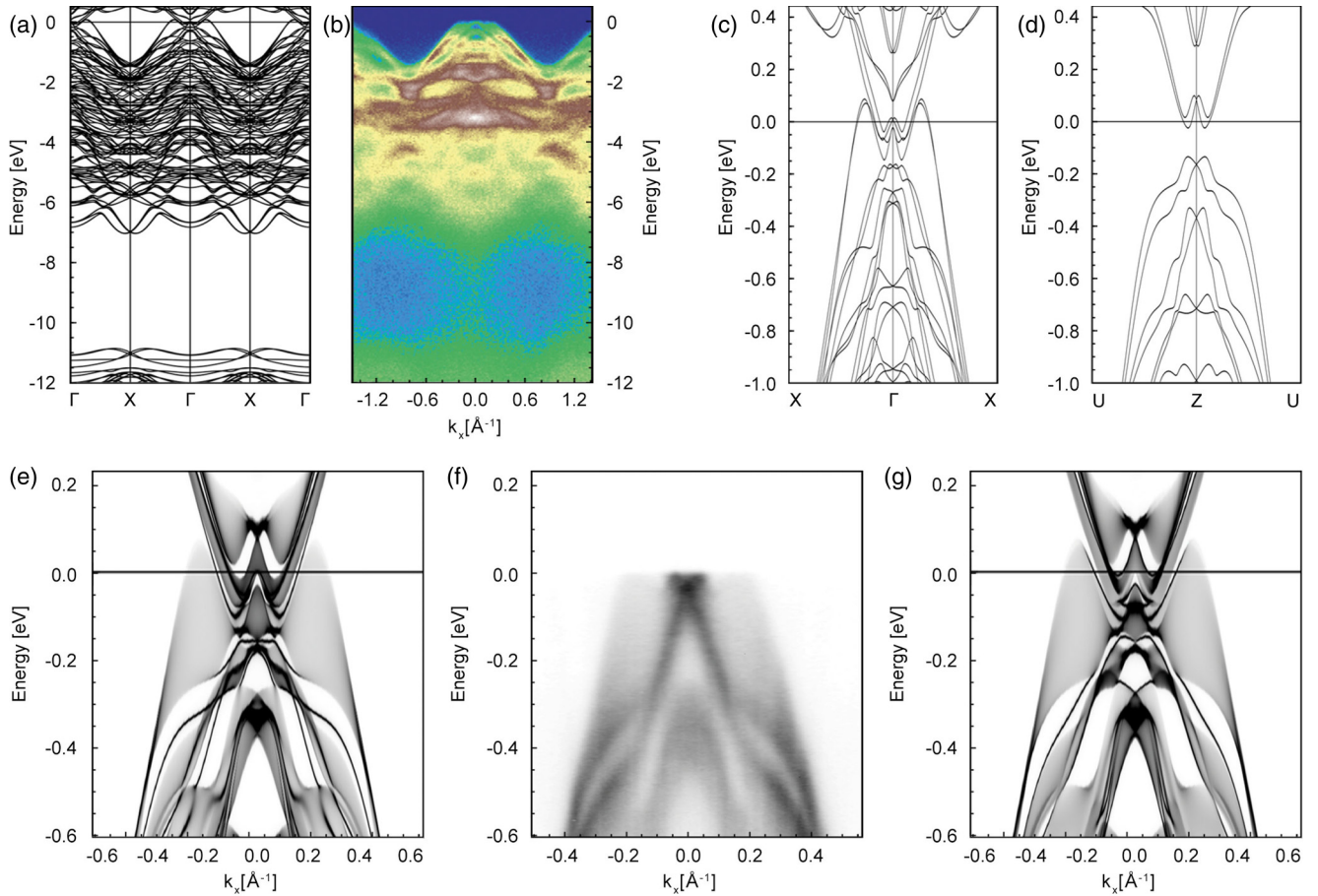
FIG. 2. (a) Band-structure calculations along X-Γ-X. (b) ARPES measurements along X-Γ-X. (c) Zoomed-in band structure along X-Γ-X. (d) Zoomed-in band structure along U-Z-U. (e) Calculated spectral function at $k_y = 0$ for the (001) surface. (f) Corresponding ARPES data taken at 99 eV photon energy. (g) Calculated spectral function at $k_y = 0$ for the (00$\bar{1}$) surface.

map is shown in Fig. 3(a) from which we can obtain the area covered by particular Fermi surface sheets. The areas of the small and large holelike pockets are approximated by red and yellow ellipses, and if calculated according to Ref. [28], are equal to $\sim$70 and $\sim$215 T, respectively. Both values are in very reasonable agreement with the corresponding frequencies ($\sim$73 and $\sim$240 T) determined in recent de Haas–van Alphen (dHvA) experiments [24]. As quantitative measures of the linear size of the large holelike and electronlike FSs, we consider the width of the momentum-distribution curve (MDC) introduced in Fig. 3(b) and the distance between the peaks of the MDC shown in Fig. 3(c), respectively. Now we can directly compare the experimental FS [Fig. 3(d)] with the Fermi surface map calculated from the spectral function for both surfaces [Figs. 3(e) and 3(f)]. From this comparison it is seen that while the size of the large hole pockets (H) along k_x is in good correspondence with the predicted value, the small holelike pockets appear to be noticeably smaller and the electronlike ones (E) larger in the calculations. To match the size of the electronlike pockets one should cut the calculated spectral function at a binding energy of 75 meV, as demonstrated in Figs. 3(h) and 3(i). However, such a shift results in the merging of all holelike pockets, which are well separated in the experiment [Figs. 3(a) and 3(d)]. In turn, the merging holelike pockets can be achieved by considering a

momentum distribution of the ARPES intensity at a 25 meV binding energy, as is seen in Fig. 3(g). In other words, while all the features are present and resemble those in the calculations, there is no single rigid shift which would result in a full quantitative agreement. In order to obtain the experimental electronic structure one needs to distort the theoretical one in a peculiar way: The electronic states making the small holelike pockets should be shifted up by $\sim$25 meV and finally the dispersions responsible for the electronlike FS should be shifted up by 75 meV. We note that such a distortion of the calculated band structure is also routinely seen in iron-based superconductors [29] and in a certain sense is more natural than the rigid shift as it can preserve the charge. From Fig. 3 we also learn that only the calculations for the (001) surface [Figs. 3(e) and 3(h)] are reproducing the experimental data, taking into account the aforementioned adjustment of different FS sheets. For example, the nearly parallel structures in the center of the Brillouin zone are only seen from the (001) surface maps and not in the (00$\bar{1}$) ones [Figs. 3(f) and 3(i)].

With the details of the electronic structure now at hand and a degree of quantitative correspondence between theory and experiment being established, we can focus on the detection of the topological surface states which support Fermi arcs connecting the Weyl points. According to the calculated spectral function [see Fig. 3(e) and Fig. 3 in Ref. [23]], these surface
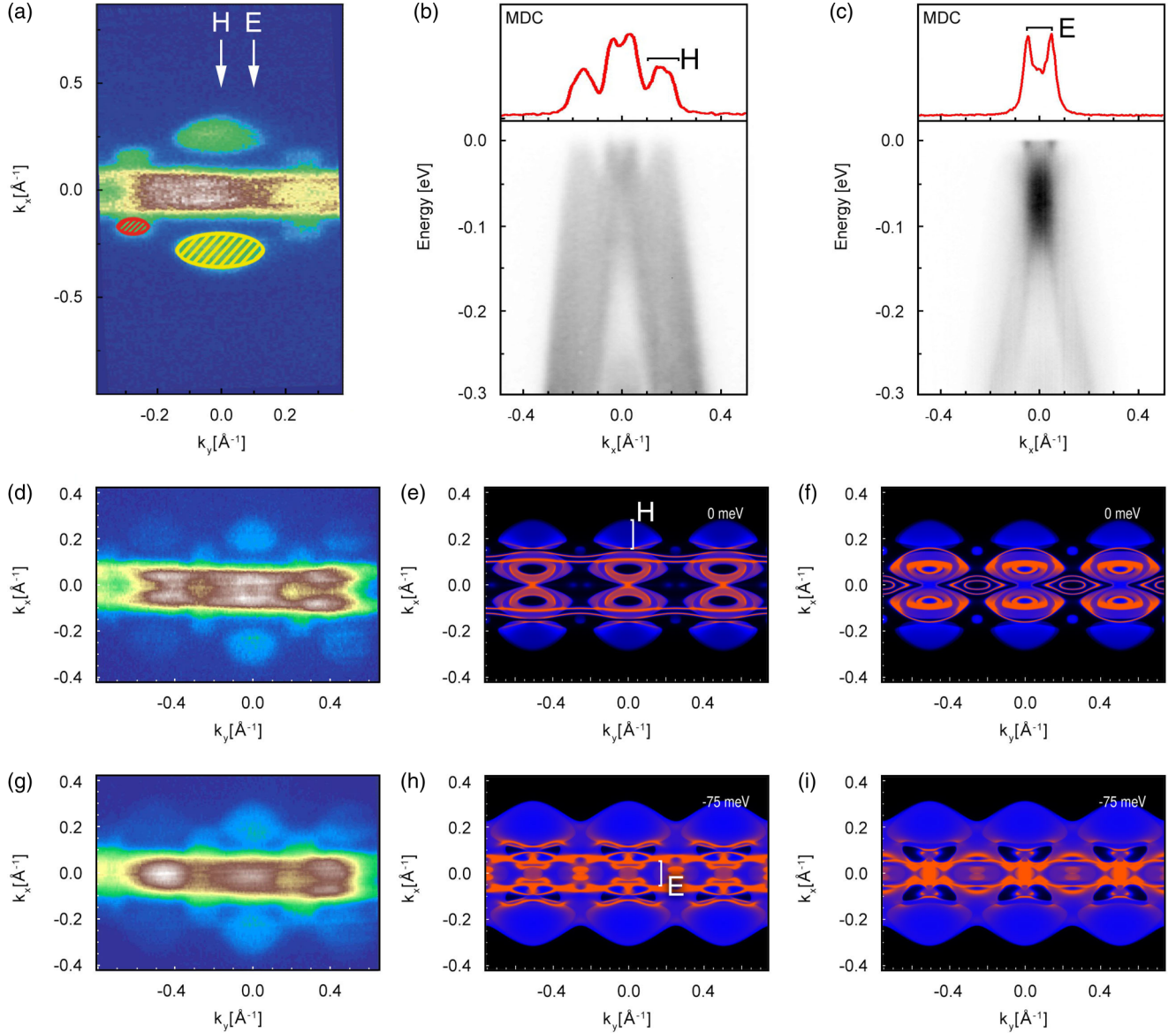
FIG. 3. (a) ARPES Fermi surface map with the shaded areas of hole pockets for comparison with dHvA. The Arrows indicate the positions of the cuts shown in (b) (*H*) and (c) (*E*). (b) and (c) ARPES momentum-energy cuts at positions shown by *H* and *E* in (a) with corresponding Fermi-level MDC curves on top. (d) ARPES Fermi surface map taken using 25 eV photons and covering three BZs. (e) Calculated Fermi surface map for the (001) surface. (f) Calculated Fermi surface map for the (00$\bar{1}$) surface. (g) ARPES momentum distribution at 25 meV below the Fermi level. (h) Calculated momentum distribution of the intensity at 75 meV binding energy for the (001) surface. (i) Calculated momentum distribution of the intensity at 75 meV binding energy for the (00$\bar{1}$) surface.

states in the case of (001) surface are located at the edge of the large holelike FS. We do observe such edges at certain k_z [e.g., the right Brillouin-zone in Fig. 3(d)], and in Fig. 4 we present more detailed and direct evidence for topological surface states supporting the Fermi arcs and the arcs themselves. In Figs. 4(a) and 4(d) we show theoretical calculated data for a cut through the Fermi arc for a position with $k_y < k_y(WP)$ [Fig. 4(a)] and for $k_y > k_y(WP)$ [Fig. 4(d)], comparing them with two experimental cuts in momentum space which cross the FS arcs, shown in Figs. 4(b), 4(c), 4(e), and 4(f). One can easily identify the topological surface states, indicated with red in Figs. 4(a) and 4(d), as sharpening of the intensity on the inner sides of the smeared out intensity corresponding to 3D dispersions of the

hole pockets. This is confirmed by the maxima in MDCs [white solid lines in Figs. 4(b) and 4(e)] and by the second-derivative plots in Figs. 4(c) and 4(f).

The agreement with the calculations is both qualitative and quantitative, as the Fermi velocity is ~1 eV Å in all cases. In Fig. 4(g) we show the second derivative of the FS map, which is similar to the right part of the one shown in Fig. 3(d). Now the Fermi arcs are seen directly and with unprecedented clarity. Also, the shape of the arcs strongly resembles the calculated ones seen at the borders of large hole pockets in Fig. 3(e).

As predicted theoretically and shown experimentally for the (001) surface, the arcs in TaIrTe$_4$ are peculiar: They are long
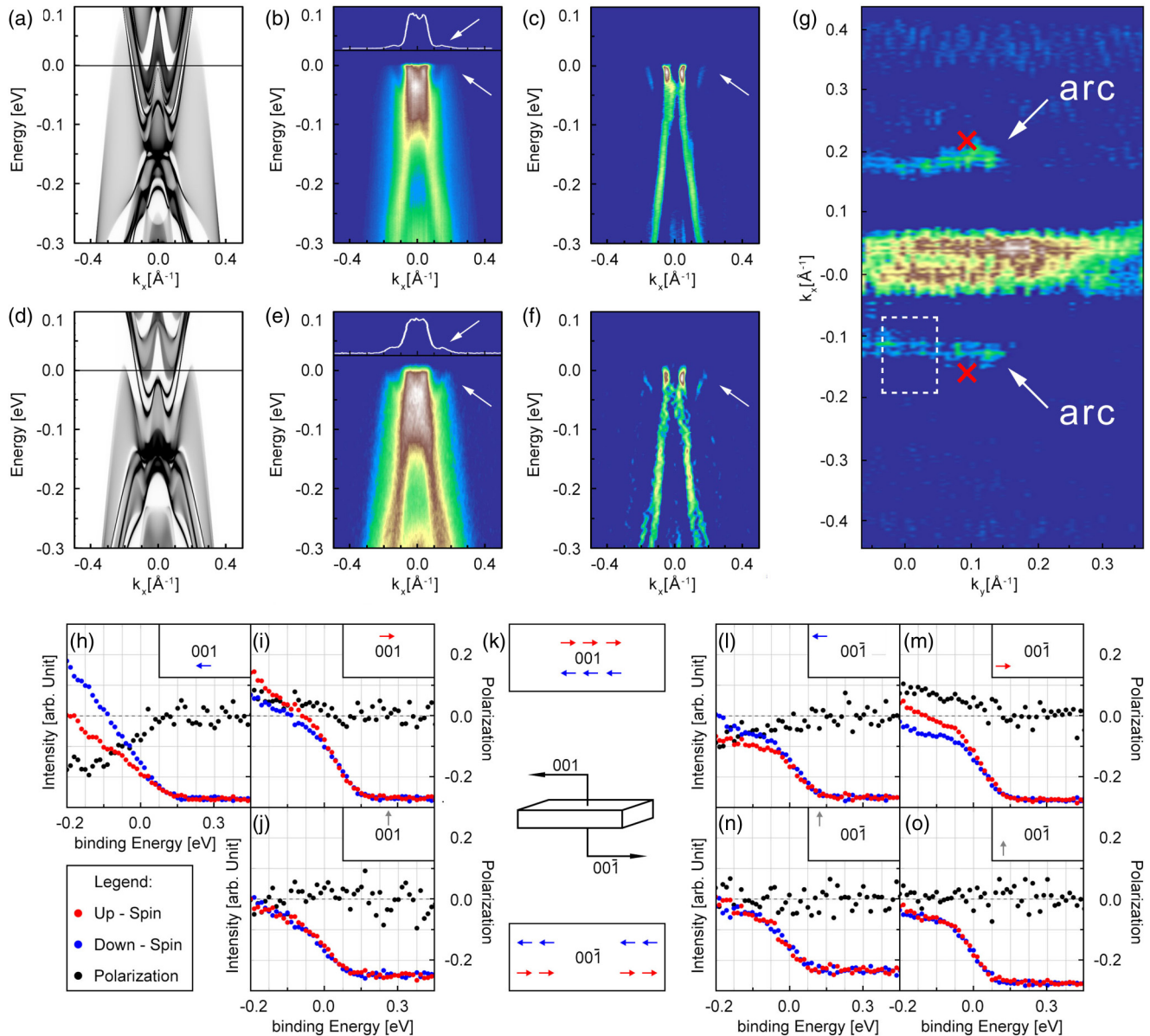
FIG. 4. (a) Spectral function calculated for $k_y = 0.05$ Å^{-1} and (d) for $k_y = 0.16$ Å^{-1}. (b), (e) Corresponding ARPES data. Peaks in MDCs and dispersing features are shown by white arrows. (c), (f) Second derivatives of (b) and (e) highlighting the presence of topological surface states. (g) Second derivative of the Fermi surface map of the second BZ, similar to the one shown in Fig. 3(d). Arcs are clearly seen and are shown by the arrows. The dashed box approximately corresponds to the typical portion of the k space probed by spin-resolved ARPES (SARPES). Weyl points are shown as red crosses and the positions of both cuts from (a)–(f) are indicated with dashed arrows. (h)–(j), (l)–(o) Spin-resolved ARPES measurements performed at the points of the k space schematically indicated by arrows next to the surface vector in the insets. (k) Schematic summary of the SARPES results. The electronic states on the arcs are spin polarized, as shown by the arrows within the BZ boundaries.

and reasonably straight. With these characteristics in mind one would obviously be interested to learn about the spin of these states from the point of view of applications in spintronics.

In Figs. 4(h)–4(n) we present the spin-resolved measurements from both surfaces of TaIrTe$_4$. We have analyzed the energy distribution curves which correspond to the topological surface states (the momentum integration window is shown in Fig. 4) in different parts of the BZ. Because of the integration over a larger portion of the k space for spin-resolved measurements, the signal contains a contribution from the bulk states. Nevertheless, this contribution is significantly smaller than that

collected from the surface state dispersion. There is always a clear signal corresponding to a particular direction of spin. The positive (negative) spin polarization of a particular portion of the arc is given by red (blue) arrows while the absence of spin polarization is indicated by gray arrows. As follows from Figs. 4(h)–4(j) for surface (001) and from Figs. 4(k)–4(n) for surface (00$\bar{1}$), the spins are always directed along the arcs and their directions are naturally opposite when k_y is inverted. We summarize our observations schematically in Fig. 4(k). We note that the spin characters of the states corresponding to the arcs are in close agreement with those which were theoretically

predicted and experimentally determined in the case of WTe_2 [22].

$TaIrTe_4$ thus emerges as a very interesting material, from both fundamental and practical points of view. Although the Weyl points themselves lie above the Fermi level, the topological surface states which support the Fermi surface arcs are clearly present and reveal a unique spin texture. Unlike the surface states of topological insulators whose spins are directed tangential to the closed FS contour, the spin texture of arcs in $TaIrTe_4$ is strongly unidirectional, implying very anisotropic spin transport properties and even the possibility of storing information. Indeed, both surfaces are characterized by states with opposite spin separated in momentum space. Taking into account the strong anisotropy of the chiral anomaly expected in a type-II Weyl semimetal, experiments in magnetic and electric fields are urgently called for.

We thus demonstrated that the predicted electronic structure of the noncentrosymmetric type-II Weyl semimetal $TaIrTe_4$ is realized experimentally. We have directly observed topological surface states and Fermi arcs with a unique spin texture, implying an enormous application potential of the material.

Note added. Recently, we became aware of pump-probe ARPES experiments on $TaIrTe_4$ which identified the Weyl points above the Fermi level, thus confirming our results [30].

[1] S. Borisenko, Q. Gibson, D. Evtushinsky, V. Zabolotnyy, B. Buechner, and R.-J. Cava, Experimental Realization of a Three-Dimensional Dirac Semimetal, Phys. Rev. Lett. **113**, 027603 (2014).

[2] M. Neupane, S. Xu, R. Sankar, N. Alidoust, G. Bian, C. Liu, I. Belopolski, T. R. Chang, H. T. Jeng, H. Lin, A. Bansil, F. Chou, and M. Z. Hasan, Observation of a topological 3D Dirac semimetal phase in high-mobility Cd_3As_2, Nat. Commun. **5**, 3786 (2014).

[3] B. Q. Lv, H. M. Weng, B. B. Fu, X. P. Wang, H. Miao, J. Ma, P. Richard, X. C. Huang, L. X. Zhao, G. F. Chen, Z. Fang, X. Dai, T. Qian, and H. Ding, Experimental discovery of Weyl semimetal TaAs, Phys. Rev. X **5**, 031013 (2015).

[4] S.-Y. Xu, I. Belopolski, N. Alidoust, M. Neupane, C. Zhang, R. Sankar, S. M. Huang, C. C. Lee, G. Chang, B. Wang, G. Bian, H. Zheng, D. S. Sanchez, F. Chou, H. Lin, S. Jia, and M. Z. Hasan, Discovery of a Weyl fermion semimetal and topological Fermi arcs, Science **349**, 613 (2015).

[5] L. Yang, Z. Liu, Y. Sun, H. Peng, H. Yang, T. Zhang, B. Zhou, Y. Zhang, Y. Guo, M. Rahn, D. Prabhakaran, Z. Hussain, S. K. Mo, C. Felser, B. Yan, and Y. Chen, Weyl semimetal phase in the noncentrosymmetric compound TaAs, Nat. Phys. **11**, 728 (2015).

[6] S. Borisenko, D. Evtushinsky, Q. Gibson, A. Yaresko, T. Kim, M. N. Ali, B. Buechner, M. Hoesch, and R. J. Cava, Time-reversal symmetry breaking type-II Weyl state in $YbMnBi_2$, arXiv:1507.04847.

[7] X. Wan, A. M. Turner, A. Vishwanath, and S. Y. Savrasov, Topological semimetal and Fermi-arc surface states in the electronic structure of pyrochlore iridates, Phys. Rev. B **83**, 205101 (2011).

[8] H. Weng, C. Fang, Z. Fang, B. A. Bernevig, and X. Dai, Weyl Semimetal Phase in Noncentrosymmetric Transition-Metal Monophosphides, Phys. Rev. X **5**, 011029 (2015).

[9] L. Balents, Viewpoint: Weyl electrons kiss, Physics **4**, 36 (2011).

[10] A. A. Soluyanov, D. Gresch, Z. Wang, Q. Wu, M. Troyer, X. Dai, and B. A. Bernevig, Type-II Weyl semimetals, Nature (London) **527**, 495 (2015).

[11] H. Nielsen and M. Ninomiya, The Adler-Bell-Jackiw anomaly and Weyl fermions in a crystal, Phys. Lett. B **130**, 389 (1983).

[12] J. Jiang, F. Tang, X. C. Pan, H. M. Liu, X. H. Niu, Y. X. Wang, D. F. Xu, H. F. Yang, B. P. Xie, F. Q. Song, X. G. Wan, and D. L. Feng, Signature of Strong Spin-Orbital Coupling in the Large Nonsaturating Magnetoresistance Material WTe_2, Phys. Rev. Lett. **115**, 166601 (2015).

[13] S. Y. Xu, N. Alidoust, G. Chang, H. Lu, B. Singh, I. Belopolski, D. Sanchez, X. Zhang, G. Bian, H. Zheng, M. A. Husanu, Y. Bian, S. M. Huang, C. H. Hsu, T. R. Chang, H. T. Jeng, A. Bansil, V. N. Strocov, S. Jia, and M. Z. Hasan, Discovery of Lorentz-violating Weyl fermion semimetal state in LaAlGe materials, arXiv:1603.07318.

[14] J. Jiang, Z. K. Liu, Y. Sun, H. F. Yang, R. Rajamathi, Y. P. Qi, L. X. Yang, C. Chen, H. Peng, C.-C. Hwang, S. Z. Sun, S.-K. Mo, I. Vobornik, J. Fujii, S. S. P. Parkin, C. Felser, B. H. Yan, and Y. L. Chen, Signature of type-II Weyl semimetal phase in $MoTe_2$, Nat. Commun. **8**, 13973 (2017).

[15] A. Liang, J. Huang, S. Nie, Y. Ding, Q. Gao, C. Hu, S. He, Y. Zhang, C. Wang, B. Shen, J. Liu, P. Ai, L. Yu, X. Sun, W. Zhao, S. Lv, D. Liu, C. Li, Y. Zhang, Y. Hu, Y. Xu, L. Zhao, G. Liu, Z. Mao, X. Jia, F. Zhang, S. Zhang, F. Yang, Z. Wang, Q. Peng, H. Weng, X. Dai, Z. Fang, Z. Xu, C. Chen, and X. J. Zhou, Electronic evidence for type II Weyl semimetal state in $MoTe_2$, arXiv:1604.01706.

[16] K. Deng, G. Wan, P. Deng, K. Zhang, S. Ding, E. Wang, M. Yan, H. Huang, H. Zhang, Z. Xu, J. Denlinger, A. Fedorov, H. Yang, W. Duan, H. Yao, Y. Wu, S. Fan, H. Zhang, X. Chen, and S. Zhou, Experimental observation of topological Fermi arcs in type-II Weyl semimetal $MoTe_2$, Nat. Phys. **12**, 1105 (2016).

[17] L. Huang, T. M. McCormick, M. Ochi, Z. Zhao, M.-T. Suzuki, R. Arita, Y. Wu, D. Mou, H. Cao, J. Yan, N. Trivedi, and A. Kaminski, Spectroscopic evidence for type II Weyl semimetal state in $MoTe_2$, Nat. Mater. **15**, 1155 (2016).

[18] N. Xu, Z. J. Wang, A. P. Weber, A. Magrez, P. Bugnon, H. Berger, C. E. Matt, J. Z. Ma, B. B. Fu, B. Q. Lv, N. C. Plumb, M. Radovic, E. Pomjakushina, K. Conder, T. Qian, J. H. Dil, J. Mesot, H. Ding, and M. Shi, Discovery of Weyl semimetal state violating Lorentz invariance in $MoTe_2$, arXiv:1604.02116.

[19] F. Y. Bruno, A. Tamai, Q. S. Wu, I. Cucchi, C. Barreteau, A. de la Torre, S. McKeown Walker, S. Riccò, Z. Wang, T. K. Kim, M. Hoesch, M. Shi, N. C. Plumb, E. Giannini, A. A. Soluyanov, and

F. Baumberger, Observation of large topologically trivial Fermi arcs in the candidate type-II Weyl semimetal WTe$_2$, Phys. Rev. B **94**, 121112(R) (2016).

[20] C. Wang, Y. Zhang, J. Huang, S. Nie, G. Liu, A. Liang, Y. Zhang, B. Shen, J. Liu, C. Hu, Y. Ding, D. Liu, Y. Hu, S. He, L. Zhao, L. Yu, J. Hu, J. Wei, Z. Mao, Y. Shi, X. Jia, F. Zhang, S. Zhang, F. Yang, Z. Wang, Q. Peng, H. Weng, X. Dai, Z. Fang, Z. Xu, C. Chen, and X. J. Zhou, Observation of Fermi arc and its connection with bulk states in the candidate type-II Weyl semimetal WTe$_2$, Phys. Rev. B **94**, 241119 (2016).

[21] Y. Wu, D. Mou, N. H. Jo, K. Sun, L. Huang, S. L. Bud'ko, P. C. Canfield, and A. Kaminski, Observation of Fermi arcs in type-II Weyl semimetal candidate WTe$_2$, Phys. Rev. B **94**, 121113(R) (2016).

[22] B. Feng, Y. H. Chan, Y. Feng, R. Y. Liu, M. Y. Chou, K. Kuroda, K. Yaji, A. Harasawa, P. Moras, A. Barinov, W. Malaeb, C. Bareille, T. Kondo, S. Shin, F. Komori, T. C. Chiang, Y. Shi, and I. Matsuda, Spin texture in type-II Weyl semimetal WTe$_2$, Phys. Rev. B **94**, 195134 (2016).

[23] K. Koepernik, D. Kasinathan, D. Efremov, S. Khim, S. Borisenko, B. Büchner, and J. van den Brink, TaIrTe$_4$: A ternary type-II Weyl semimetal, Phys. Rev. B **93**, 201101 (2016).

[24] S. Khim, K. Koepernik, D. V. Efremov, J. Klotz, T. Förster, J. Wosnitza, M. I. Sturza, S. Wurmehl, C. Hess, J. van den Brink, and B. Büchner, Magnetotransport and de Haas–van Alphen measurements in the type-II Weyl semimetal TaIrTe$_4$, Phys. Rev. B **94**, 165145 (2016).

[25] T. Okuda, K. Miyamaoto, H. Miyahara, K. Kuroda, A. Kimura, H. Namatame, and M. Taniguchi, Efficient spin resolved spectroscopy observation machine at Hiroshima Synchrotron Radiation Center, Rev. Sci. Instrum. **82**, 103302 (2011).

[26] T. Okuda, K. Miyamoto, A. Kimura, H. Namatame, and M. Taniguchi, A double VLEED spin detector for high-resolution three-dimensional spin vectorial analysis of anisotropic Rashba spin splitting, J. Electron Spectrosc. Relat. Phenom. **201**, 23 (2015).

[27] K. Koepernik and H. Eschrig, Phys. Rev. B **59**, 1743 (1999).

[28] L. Onsager, Interpretation of the de Haas–van Alphen effect, London, Edinburgh Dublin Philos. Mag. J. Sci. **43**, 1006 (1952).

[29] S. V. Borisenko, D. V. Evtushinsky, Z.-H. Liu, I. Morozov, R. Kappenberger, S. Wurmehl, B. Büchner, A. N. Yaresko, T. K. Kim, M. Hoesch, T. Wolf, and N. D. Zhigadlo, Direct observation of spin-orbit coupling in iron-based superconductors, Nat. Phys. **12**, 311 (2016).

[30] I. Belopolski, P. Yu, D. S. Sanchez, Y. Ishida, T. R. Chang, S. S. Zhang, S. Y. Xu, D. Mou, H. Zheng, G. Chang, G. Bian, H. T. Jeng, T. Kondo, A. Kaminski, H. Lin, Z. Liu, S. Shin, and M. Z. Hasan, A minimal, "hydrogen atom" version of an inversion-breaking Weyl semimetal, arXiv:1610.02013.